


Insights into Fano-type resonance fluorescence from quantum-dot–metal-nanoparticle molecules with a squeezed vacuum

Shuting Shen^{✉,*}, Zhiming Wu, Jiahua Li^{✉,†} and Ying Wu[‡]

School of Physics, Huazhong University of Science and Technology, Wuhan 430074, People's Republic of China

 (Received 9 April 2021; accepted 7 July 2021; published 21 July 2021)

Metal nanoparticles (MNPs) possess the intriguing property of enhancing and limiting the energy of light field to subwavelength scale, which have attracted extensive attention in physics, chemistry, and life sciences. Meanwhile, squeezing is a general concept in quantum optics and can be used to engineer matter interaction scenarios. Here we consider an artificial hybrid molecule consisting of an MNP interacting with a semiconductor quantum dot (QD), combining with a squeezed reservoir. Using experimentally realistic parameters for the MNP-QD architecture and fully quantized approach, we theoretically explore the optical properties of the hybrid molecule driven by an external applied laser field via probing the resonance fluorescence in the steady state. We show that in this way it is possible to engineer and control the peak-value magnitudes, widths, and shapes of the resonance fluorescence spectra under the influence of the squeezed vacuum field without the need for the strong-coupling condition between the MNP and QD. In particular, some interesting phenomena in rich spectral responses are attainable, including Fano-type resonance fluorescence, fluorescence quenching, fluorescence narrowing, and fluorescence enhancement. Our method can also be extended to other nanoscopic structures, such as a plasmonic nanoantenna coupled to an emitter. These unique line shapes obtained here may have potential applications in developing quantum plasmonic platforms and sensitive on-chip devices such as optical switches and sensors.

DOI: [10.1103/PhysRevA.104.013717](https://doi.org/10.1103/PhysRevA.104.013717)

I. INTRODUCTION

It is known that localized surface plasmons (LSPs) are nonpropagating excitations generated by the coupling of conduction electrons in metal nanoparticles (MNPs) of sub-wavelength size with an external electromagnetic field, which are essentially owing to the collective oscillation of the free electrons in the conduction band near the Fermi level on the metal surface driven by the electromagnetic field [1–3]. When the frequency of the external electromagnetic field is close to that of the LSP, the localized surface plasmon resonance (LSPR) occurs, which results in the energy of the electromagnetic field being effectively transformed into the electromechanical energy of the free electrons on the metal surface [4]. Thus, an intriguing capability of the MNP is their ability to concentrate and enhance the optical energy at the nanoscale by supporting the LSPRs [5,6].

The concentration of light energy at nanometer level enables the MNP to be used as metallic nanocavity [7], which not only overcomes the limitation of half wavelength size of the conventional optical cavities, but also facilitates the scalable and ultracompact integration compared with the conventional micron-size optical cavities [8–10]. Strong electromagnetic field localization and enhancement in or near the MNP can significantly enhance the light-matter inter-

action, which has received extensive attention in a wide range of contexts [11–15], such as surface-enhanced Raman scattering [16,17], biosensing [18], and so on. The interaction between the MNP and gain system is an important subject in photonics and optoelectronics [19]. Among them, the hybridization of the MNP and solid-state quantum dot (QD) can produce fascinating optical phenomena, including Fano resonance [2,20–22], tailored resonance fluorescence or spontaneous emission [23–31], controlled quantum statistics [2,8,32–37], cloaking [38], squeezing [39,40], and so on, which has many potential applications in ultrasensitive spectroscopy [41], nanoscale refractive index sensing [8], biosensors [18,42], spaser [7,43,44], optoelectronic nanodevices [45–49], single photon source [50–56], and other fields. The hybrid MNP-QD system not only has the high openness that can cause the interference between the scattered fields of the MNP and QD [2,8], but also has the controllability that can manipulate the optical properties by adjusting their size and structure [3,57]. Nowadays, the improved nanofabrication methods can efficiently control the shape of the MNP and the arrangement of the MNP ensembles, and provide the possibility to flexibly customize specific molecular-MNP coupling [58,59], which increase the feasibility of experimental implementation of the hybrid MNP-QD system model.

For the spherical MNP, its electromagnetic characteristics can be reflected by its angular momentum, i.e., n [29]. When the dimension of the MNP is assumed to be much smaller compared to the incident light wavelength λ ($r_m \ll \lambda$, with r_m being the MNP radius), the dipole approximation is valid due to the optical response of the MNP can be determined

*shenst1995@163.com

†Corresponding author: huajia_li@163.com

‡yingwu2@126.com

by the dipole mode ($n = 1$). However, when the QD is too close to the MNP, the higher modes ($n > 1$) need to be taken into account, which leads to rich optical effects, for example, quantum statistics control [8], strong coupling and quenching [29], and so on. Similar to the literatures [2,3,9], we study only the dipole-dipole interaction between the MNP and QD in the hybrid system, so the situation of occurring multimode effects should be avoided [60–63]. Besides, in order to ensure that there is no direct tunneling between the MNP and QD, the QD must be placed at a distance of more than 2 nm from the MNP surface ($d - r_m > 2$ nm, with d being the center-to-center distance between the MNP and QD) [2,9,64]. In the following discussion, we consider the case where the QD is placed at a distance greater than $2r_m$ from MNP, which is sufficient to ignore the high-order multipole and avoid the direct tunneling effect.

The nonclassical electromagnetic field state–squeezed state can be produced in many nonlinear optical processes [65–71], which has a wide range of applications in quantum information processing, ultrasensitive electronics and quantum metrology [72]. Previously, the interaction between a squeezed vacuum and atomic systems has been studied widely [73–75], and many interesting optical phenomena have been obtained, such as anomalous resonance fluorescence [76], subnatural linewidth narrowing [74,77], two-photon excitation [78–81], and so on. Since the standard technique for producing a squeezed vacuum has been available for decades [81,82], it is feasible to explore the interaction of nonclassical light with matter using existing laboratory techniques. Among growing interest in employing quantum states of light in nanoplasmonic applications, several groups [83–85] have experimentally reported that both surface plasmon polaritons (SPPs) and LSPs are capable of coherently transducing the single-mode and multimode squeezed states of light, where the squeezing loss equivalent to the plasmonic loss can be modeled by an effective beamsplitter interaction. Even though the decoherence caused by collisions among millions of electrons that constitute the plasmons, quantum properties through SPPs and LSPs, for example, the quadrature squeezed vacuum states [83] and intensity-difference squeezed states [84] of plasmonic modes, can be basically preserved in the photon-SPP(LSP)-photon conversion process. To our knowledge, no further theoretical or experimental work has been done to investigate the optical properties of hybrid MNP-QD systems driven by a squeezed vacuum field, which has inspired the current research.

In this work, we study the optical fluorescence properties of the hybrid MNP-QD molecule under the influence of a squeezed vacuum field, focusing on the weak-coupling regime of MNP-QD. Under the excitation of an external applied field, the MNP as an open nanocavity can lead to the interference between the MNP and QD scattered light in the hybrid system. The previous studies [86–90] have clearly shown that engineering the vacuum fluctuations can be utilized to control the strength and the range of matter interactions. Consequently, the key element of our approach is a squeezed vacuum field that achieves the squeezed-vacuum-enhanced MNP-QD interactions [87,89]. In the absence of the squeezed vacuum field, the steady-state emission power spectral density (i.e., fluorescence spectrum) of the hybrid molecule presents a

monotonic Lorentzian-like profile. Contrarily, in the presence of the squeezed vacuum field, the generated fluorescence spectra can exhibit rich and typical characteristics under realistic conditions. In detail, it is found that the introduction of the squeezed vacuum field can engineer and tailor the peak-value magnitudes, widths, and shapes of the resonance fluorescence. In addition, the results also indicate that, by properly adjusting the system parameters, such as the squeezing parameter, the frequency detuning between the MNP and QD, the center-to-center distance between the MNP and QD, the MNP radius, and the polarization direction of the applied electromagnetic field, we can succeed in catching some interesting phenomena in the emission power spectra, including Fano-type resonance fluorescence, fluorescence quenching, fluorescence narrowing, and fluorescence enhancement. We also assess the feasibility of the scheme using currently available technology. As an alternative scheme with nanoscale footprint, this work provides more adjustable parameters (degrees of freedom) for us to control the emission power spectra, which can be expected to find potential applications in on-chip photonic devices such as optical switches, low-threshold lasers, and sensitive sensors.

The remainder of the paper is organized as follows: In Sec. II, starting from describing the physical model of the hybrid MNP-QD system under consideration, the total Hamiltonian of the hybrid system is given. Subsequently, the quantum master equation of the hybrid MNP-QD system is yielded. Furthermore, we derive the expression of the total polarization operator which contains the key information we need. In Sec. III we briefly demonstrate the experimental feasibility and the choice of a set of system parameters of the hybrid MNP-QD molecule. In Sec. IV we analyze and discuss in detail the dependence of the optical properties of the hybrid MNP-QD system on the system parameters. Finally, conclusions are given Sec. V.

II. THEORETICAL MODEL AND BASIC EQUATIONS

As depicted schematically in Fig. 1, we consider a hybrid molecule composed of a two-level QD and a spherical MNP with radius r_m . The MNP and QD are separated by a center-to-center distance d and embedded in a homogenous dielectric medium with permittivity ϵ_b . The hybrid molecule is subject to both an external driving field $E_{\text{dri}} = E_0 e^{-i\omega_d t} + \text{c.c.}$ (E_0 being the amplitude, ω_d being the angular frequency, and c.c. denoting the complex conjugation) and a broadband squeezed vacuum E_{squ} . The polarization of the applied external electric field is along the axis joining the MNP and QD structure.

The MNP has the excellent optical property that can support the LSPs, enabling it to enhance and focus optical fields to the subwavelength ranges [1]. For single-valence plasmonic metals (such as silver, gold, copper, alkaline metals), the skin depth l_s of the metals is about 25 nm over the entire optical region [4]. About small-scale MNP with $r_m \leq l_s$, the external light field can penetrate the whole MNP and drive the collective oscillations of electrons, which enables the MNP to localize the electromagnetic energy in the form of electromechanical energy at the nanoscale. For the magnitude of the MNP is much smaller than the wavelength λ of the incident light ($r_m \ll \lambda$) (it is obvious

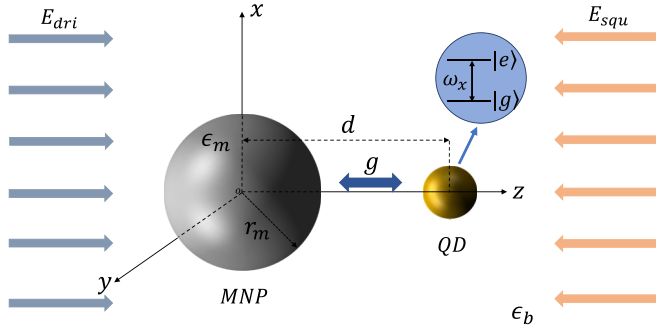


FIG. 1. Schematic of the hybrid system composed of a spherical MNP and a QD embedded in a homogeneous dielectric medium with relative permittivity ϵ_b (vacuum here, $\epsilon_b = 1$). Both the MNP and the two-level QD (with the excited state $|e\rangle$ and the ground state $|g\rangle$, ω_x being the transition frequency of the QD) are driven by an external electric field E_{dri} . In order to more clearly describe the polarization direction of the applied electric field, we define the major axis of the hybrid MNP-QD system as parallel to the z axis. Besides, the hybrid system also interacts with a squeezed vacuum E_{squ} . In the hybrid MNP-QD system, there is no direct tunneling interaction between the MNP and QD. The coupling between the LSP in MNP and the exciton in QD is due to the long-range Coulomb interaction, which causes the formation of hybrid molecule and promotes energy transfer [13,21]. The coupling strength between the MNP and QD is parameterized by g . Other symbols are defined and explained in the main text.

that the condition $r_m \ll \lambda$ is automatically satisfied when $r_m \leq l_s$, the quasistatic approximation is an effective approximation method to solve the interaction between the MNP and incident light field [91].

The quasistatic approximation allows that the incident light field is approximately uniform over the entire MNP sphere, considering only the time dependence of the oscillating electromagnetic field and ignoring its spatial dependence. In the quasistatic regime, it is effective to treat the MNP as an ideal dipole for the reason that the incident field can couple only to the dipole moment of the MNP but not to higher order multipoles [2,8]. When considering the hybrid MNP-QD system, the dipole approximation is still valid when the distance between the MNP and QD is far enough. On the other hand, the QD can be viewed as a pointlike two-level system with the excited state $|e\rangle$ and the ground state $|g\rangle$ (see the inset of Fig. 1). Driven by the external laser, the QD senses the superposition field which is composed of the external electric field and the polarized electric field generated by the MNP. At the same time, the polarized electric field caused by the QD will also be felt by the MNP, resulting in the self-feedback formation between these fields in the hybrid MNP-QD system. In the hybrid system, we use the coupling mechanism of the dipole-dipole interaction between the LSP in the MNP and the exciton in the QD to investigate the optical response of the whole system driven by the external field.

Under the excitation of an external electric field E_{dri} , the total Hamiltonian of our coupled quantum system in the dipole and rotating-wave approximations can be written as

$$H_{\text{tot}} = H_0 + H_{\text{int}} + H_{\text{dri}}. \quad (1)$$

The specific meanings of each term in Eq. (1) are listed as follows.

The first term on the right-hand side (RHS) of Eq. (1), associated with the unperturbed Hamiltonian H_0 of the isolated MNP and QD, can be expressed as

$$H_0 = \hbar\omega_m a^\dagger a + \hbar\omega_x \sigma^\dagger \sigma, \quad (2)$$

where ω_m is the surface plasmon resonance frequency of the MNP. The spatial dielectric function of the MNP is given by $\epsilon_m(\omega) = \epsilon_\infty - \frac{\omega_p^2}{\omega^2 + i\kappa\omega}$, resulting in the relation $\omega_m = \frac{\omega_p}{\sqrt{2\epsilon_b + \epsilon_\infty}}$. Here ω_p is the plasma frequency of the metal, ϵ_∞ is the ultraviolet permittivity of metal, and ϵ_b is the relative permittivity of the homogenous dielectric that the hybrid MNP-QD system is embedded. The corresponding derivation about ω_m is carried out in Appendix A. a^\dagger and a are the creation and annihilation operators for the MNP plasmonic field mode, satisfying the bosonic commutation relation $[a, a^\dagger] = 1$. To keep the notation as simple as possible, we removed the hat of the operator. $|e\rangle$ and $|g\rangle$ represent the excited and ground states of the two-level QD. $\sigma^\dagger = |e\rangle\langle g|$ and $\sigma = |g\rangle\langle e|$ are the dipole raising and lowering operators of the two-level QD, satisfying the fermionic anticommutation relation $\{\sigma^\dagger, \sigma\} = 1$. ω_x is the transition frequency of the QD exciton-to-ground states $|e\rangle \Leftrightarrow |g\rangle$, where the energy of the ground state $|g\rangle$ is set as zero for the sake of simplicity. Also, the zero-point energy for the free MNP Hamiltonian has been ignored, which is allowed because it gives only a relative shift and does not modify the MNP-QD system dynamics under study.

The second term on the RHS of Eq. (1), associated with the dipole-dipole interaction Hamiltonian H_{int} between the MNP and QD, can be written as

$$H_{\text{int}} = i\hbar g(a^\dagger \sigma - a \sigma^\dagger), \quad (3)$$

where g is the coupling strength between the MNP plasmonic field mode and the two-level QD, following the relationship $\hbar g = \mu \epsilon$. Here μ is the transition dipole moment of the two-level QD, which is assumed to be real without loss of generality. The positive-frequency component of the dipole response field created by the surface plasmon mode of the MNP oscillating as $e^{-i\omega t}$ felt by the QD, $E_m^+ = i\epsilon a$ is due to the induced polarization of the MNP under the external field. The derivation of the specific expression of the coefficients g and ϵ above is given in Appendix B.

The third term on the RHS of Eq. (1) accounts for the dipole interaction of the MNP and QD with the external driving field E_{dri} , yielding

$$H_{\text{dri}} = -E_0 \mu (\sigma^\dagger e^{-i\omega_d t} + \sigma e^{i\omega_d t}) - E_0 (\chi a^\dagger e^{-i\omega_d t} + \chi^* a e^{i\omega_d t}), \quad (4)$$

where E_0 is the amplitude of the external driving field, ω_d is the frequency of the external driving field, and χ is the dipole moment of the MNP.

In order to eliminate the time dependence in the Hamiltonian under the Schrödinger picture, we can convert it into the interaction picture by applying a unitary manipulation. To do this, we translate the above total Hamiltonian (1) of the hybrid MNP-QD system into a rotating reference frame (interaction picture) with respect to the external driving field frequency

ω_d . For this purpose, the unitary operator is chosen as

$$U(t) = e^{-i\omega_d t(a^\dagger a + \sigma^\dagger \sigma)}. \quad (5)$$

And then, through the unitary transformation formula, namely,

$$H_{eff} = U^\dagger(t)H_{tot}U(t) - i\hbar U^\dagger(t)\frac{\partial U(t)}{\partial t}, \quad (6)$$

we can finally derive a time-independent effective Hamiltonian of the system in the interaction picture after some algebra, in the form of

$$H_{eff} = \hbar\Delta_m a^\dagger a + \hbar\Delta_x \sigma^\dagger \sigma + i\hbar g(a^\dagger \sigma - a\sigma^\dagger) - E_0\mu(\sigma^\dagger + \sigma) - E_0(\chi a^\dagger + \chi^* a), \quad (7)$$

where the notation $\Delta_m = \omega_m - \omega_d$ represents the detuning of the plasmon resonance frequency ω_m of the MNP from the frequency ω_d of the external driving laser. $\Delta_x = \omega_x - \omega_d = \omega_m + \Delta - \omega_d$ represents the detuning of the exciton resonance frequency ω_x of the two-level QD from the frequency ω_d of the external driving laser. Here the notation $\Delta = \omega_x - \omega_m$ is the detuning of the exciton resonance frequency ω_x of the two-level QD from the plasmon resonance frequency ω_m of the MNP.

It is pointed out that the above Hamiltonian (1) characterizes a closed quantum system, which does not consider any losses of the MNP-QD system due to the interaction with the external environment. In reality, when taking into account the influence of the environment or reservoir, the system will be coupled with the environment to construct an open quantum system of irreversible dynamics. In the present study, we mainly concentrate on the hybrid system interacting with a squeezed vacuum E_{squ} (see Fig. 1), which can be achieved by the action of the unitary squeezing operator $S(\xi) = \exp[\frac{1}{2}(\xi^* a^2 - \xi a^{\dagger 2})]$ on the vacuum state, rather than the vacuum or thermal reservoir [76]. Above $\xi \equiv r e^{i\phi}$ represents the squeezing parameter, in which the squeezing strength r describes the degree of squeezing and its value range is $0 \leq r < \infty$ and the squeezing angle ϕ represents the direction of squeezing and its value range is $0 \leq \phi \leq 2\pi$ [92].

In order to treat the incoherent processes and describe the complete dynamics of the MNP-QD system with the density matrix operator ρ , we can employ the Lindblad master equation under the Born-Markovian and secular approximations [92]

$$\frac{d\rho}{dt} = -\frac{i}{\hbar}[H, \rho] + L_{field}(\rho) + L_{QD}(\rho), \quad (8)$$

where

$$L_{field}(\rho) = N\frac{\kappa}{2}(2a^\dagger \rho a - a a^\dagger \rho - \rho a a^\dagger) + (N+1)\frac{\kappa}{2}(2a \rho a^\dagger - a^\dagger a \rho - \rho a^\dagger a) - M\frac{\kappa}{2}(2a \rho a - a a \rho - \rho a a) - M^*\frac{\kappa}{2}(2a^\dagger \rho a^\dagger - a^\dagger a^\dagger \rho - \rho a^\dagger a^\dagger) \quad (9)$$

and

$$L_{QD}(\rho) = N\frac{\gamma}{2}(2\sigma^\dagger \rho \sigma - \sigma \sigma^\dagger \rho - \rho \sigma \sigma^\dagger) + (N+1)\frac{\gamma}{2}(2\sigma \rho \sigma^\dagger - \sigma^\dagger \sigma \rho - \rho \sigma^\dagger \sigma) - M\frac{\gamma}{2}(2\sigma \rho \sigma - \sigma \sigma \rho - \rho \sigma \sigma) - M^*\frac{\gamma}{2}(2\sigma^\dagger \rho \sigma^\dagger - \sigma^\dagger \sigma^\dagger \rho - \rho \sigma^\dagger \sigma^\dagger) + \frac{\gamma_{dph}}{2}(2\sigma^\dagger \sigma \rho \sigma^\dagger \sigma - \sigma^\dagger \sigma \rho - \rho \sigma^\dagger \sigma). \quad (10)$$

Above, the effect of the squeezed vacuum field is represented by the parameters N , M , and ϕ , respectively. These are closely related to the squeezing parameter $\xi \equiv r e^{i\phi}$ in the following way [92]: $N = \sinh^2(r)$ and $M = \sinh(r) \cosh(r) e^{-i\phi}$, with N being the mean number of photons in the squeezed vacuum and M denoting the intensity of the two-photon correlation [93]. The squeezed vacuum reservoir degenerates into an ordinary vacuum reservoir when $N = |M| = 0$. And the squeezed vacuum reservoir degenerates into a normal thermal radiation reservoir when $N \neq 0$ and $|M| = 0$ [94]. In order to achieve the maximum effects of squeezing, we assume $|M| = \sqrt{N(N+1)}$, which is the maximum allowable value of $|M|$ [76]. In what follows, we will explore the influence of the squeezed vacuum on the optical properties of the hybrid MNP-QD system with the squeezing strength r and the squeezing phase ϕ as the variables. Here $\kappa = \kappa_r + \kappa_{nr}$ and γ are the decay rates of the MNP and the QD, respectively. κ_r is the radiation loss caused by radiation to the far field, and κ_{nr} is the nonradiation loss caused by Ohmic loss. Last, γ_{dph} is the dephasing rate of the QD.

Starting from the quantum master equation, the coupled equation of motion for the expectation values of the MNP plasmonic field can be obtained as

$$\frac{\partial}{\partial t}\langle a \rangle = \frac{\partial}{\partial t}\text{Tr}(a\rho) = \text{Tr}\left(a\frac{\partial}{\partial t}\rho\right). \quad (11)$$

By substituting Eqs. (7) and (8) into Eq. (11), and using the appropriate commutation relations, we can find

$$\frac{\partial}{\partial t}\langle a \rangle = -\left(i\Delta_m + \frac{\kappa}{2}\right)\langle a \rangle + g\langle \sigma \rangle + \frac{iE_0\chi}{\hbar}. \quad (12)$$

In the same way as above, the coupled equation of motion for the expectation value of the excitonic transition operator determining the QD polarization can be yielded as

$$\frac{\partial}{\partial t}\langle \sigma \rangle = \frac{\partial}{\partial t}\text{Tr}(\sigma\rho) = \text{Tr}\left(\sigma\frac{\partial}{\partial t}\rho\right), \quad (13)$$

from which, after a series of calculations, we can get

$$\begin{aligned} \frac{\partial}{\partial t}\langle \sigma \rangle = & -\left[i\Delta_x + (2N+1)\frac{\gamma}{2} + \frac{\gamma_{dph}}{2}\right]\langle \sigma \rangle - g\langle a \rangle \\ & + 2g\langle a\sigma^\dagger \sigma \rangle + \frac{iE_0\mu}{\hbar}(1 - 2\langle \sigma^\dagger \sigma \rangle) \\ & - M^*\gamma\langle \sigma^\dagger \rangle. \end{aligned} \quad (14)$$

From Eq. (12), we can achieve the analytical solution of a in the steady state by setting the left side of Eq. (12) to zero,

$$\langle a \rangle = \frac{g\langle \sigma \rangle}{i\Delta_m + \frac{\kappa}{2}} + \frac{iE_0\chi}{\hbar(i\Delta_m + \frac{\kappa}{2})}. \quad (15)$$

In the weak driving field limit, the number of excitons in QD can be approximately neglected, i.e., $\langle \sigma^\dagger \sigma \rangle \ll 1$, we can acquire

$$\langle \sigma \rangle = \frac{-g\langle a \rangle + \frac{iE_0\mu}{\hbar} - M^*\gamma\langle \sigma^\dagger \rangle}{i\Delta_x + (2N + 1)\frac{\gamma}{2} + \frac{\gamma_{\text{dph}}}{2}}. \quad (16)$$

In Appendix B we compare the results of the described system under the quantum framework with those predicted by the classical theory. To this end, we can figure out the parameters g and χ , with the relations

$$g = \frac{S_a\mu}{d^3} \sqrt{\frac{3r_m^3\eta}{4\pi\epsilon_0\hbar}}, \quad (17)$$

$$\chi = -i\epsilon_b \sqrt{12\eta\epsilon_0\pi\hbar r_m^3}. \quad (18)$$

After the determination of both g and χ , the expression of the total polarization operator P can be determined accordingly by

$$P = \chi^* a + \mu \sigma. \quad (19)$$

The resonance fluorescence of the hybrid MNP-QD system of interest is yielded by the power spectral density. Given the first-order correlation function $\langle P^\dagger(\tau)P(0) \rangle$, we can define the corresponding power spectral density, which is calculated as the Fourier transformation of the first-order correlation function [92,95],

$$S(\omega) = \int_{-\infty}^{+\infty} \langle P^\dagger(\tau)P(0) \rangle e^{-i\omega\tau} d\tau, \quad (20)$$

in the steady state ($t \rightarrow \infty$). With this, the fluorescence spectrum $S(\omega)$ is evaluated by using the quantum regression theorem [96] and further by solving numerically the full master equation (8) within a truncated space, as discussed more fully in Sec. IV. The analytical results are too complicated to compute here. Finally, worth to note is that all the calculations are performed in the rotating frame at the driving field frequency ω_d .

III. EXPERIMENTAL FEASIBILITY CONSIDERATION WITH CURRENT TECHNOLOGY

The experimental feasibility of the physical model and a series of selected system parameters are commented in this section. Semiconductor QDs, known as artificial atoms, have discrete energy spectra. Among them, colloidal QDs as a subset of semiconductor nanocrystals, can be chemically synthesized by means of inexpensive and scalable, wet-chemical synthetic procedures [97]. The colloidal QDs produced by this method have the advantages of smaller particle size (typically 1–10 nm in radius) and improved surface passivation. For example, the colloidal CdSe QDs can significantly inhibit surface trapping and their emission wavelengths can be tuned across the entire visible spectrum [98]. Since the particle size is closely related to the band gap energy of the colloidal QDs

and advanced semiconductor synthesis methods can support the colloidal QDs with tunable size and shape [97], which provides a prerequisite for us to achieve the required near resonance between the QD and silver (Ag) MNP by selecting the colloidal CdSe QD of appropriate size. As shown in Ref. [99], single colloidal CdSe QD with 1 nm size has an energy gap of about 2.9 eV. Again, one, two and multiple CdSe QDs can be prepared and manipulated in the experiments [100,101].

Advanced electron-beam lithography and template-stripping technology can be used to fabricate the Ag MNP [102,103]. Using chemically synthesized components and directed assembly, i.e., self-assembly scheme based on the DNA origami technique [22,104–106], the QD can be placed in the vicinity of the MNP at a controllable nanometer scale distance [107]. The MNP-QD distance in the hybrid molecule can be determined by the number of DNA base pairs, and the size of MNP can be manipulated using hydroxyl amine as the reducing agent [108]. This precise arrangement enables us to form a controllable hybrid molecule, which increases the possibility of studying the MNP-QD coupling in detail. Alternatively, using the technique of atomic force microscope (AFM) nanomanipulation [109], the MNP-QD hybrid molecule also can be assembled into a well-controlled geometry, which enables us to customize the size of individual structures and manipulate the QD position within the nanometer range. As shown in Ref. [110], using AFM nanomanipulation, the experimental method for positioning a single Au nanoparticle near a CdSe QD to construct a hybrid nanostructure with variable geometry has been proposed. Under a femtosecond-pulsed laser excitation, a single colloidal CdSe QD (average core radius: 2.6 nm) interacting with the LSPR of an Ag nanoparticle has been experimentally reported [111]. These findings above can satisfy the involved requirements needed for realizing our proposal. Compared with the traditional cavity quantum electrodynamics (QED) system, this flexible ultracompact hybrid molecule in nanoscale has the advantage of low-cost assembly methods.

Next, as early as the 1990s, scientists mastered the standard methods of experimental preparation of squeezed states, which can be exploited to reduce the experimental noise below the shot-noise limit [68]. With the increasing application of nanoscale plasmonics, including subwavelength photonic circuits and nanometer imaging, growing interest in coupling quantum light sources to plasmonic elements has been stimulated [83–85]. It is naturally proposed whether squeezed states can be applied to surface plasmon with picosecond decay and decoherence. To explore this problem, Huck *et al.* used a squeezed vacuum state to excite an electron resonance on the surfaces of a metallic gold waveguide to form a SPP [83]. And they demonstrated the transduction of single mode squeezed light into SPP despite linear loss and decoherence in the plasmonic mode. Besides, in order to demonstrate the viability of coupling quantum information into surface plasmons, Lawrie *et al.* also provided the demonstration of the transduction of a squeezed light source into LSPs [84]. This fulfills our requirement for squeezing the plasmonic vacuum of an MNP. For more details about the squeezed surface plasmons in the experiment, we refer the reader to Refs. [83–85].

Before proceeding any further, for the calculations we choose the parameters of the Ag MNP according to the

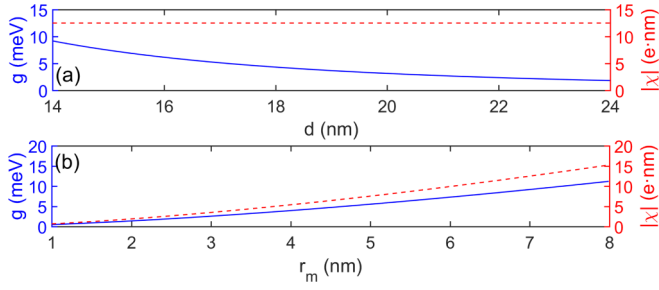


FIG. 2. (a) The coupling strength g between the MNP and QD and the modulus of the complex dipole moment χ of the MNP as a function of the MNP-QD center-to-center distance d when $r_m = 7$ nm. (b) The coupling strength g between the MNP and QD and the modulus of the complex dipole moment χ of the MNP as a function of the MNP radius r_m when $d = 14$ nm. Other unspecified system parameters have been set to $S_\alpha = 2$, $\mu = 0.7e$ nm, $\epsilon_b = 1$, $\omega_p = 7418.71$ meV, $\kappa = 53.28$ meV, and $\epsilon_\infty = 4.6$, respectively. In each pane, the blue solid line corresponds to the left axis, and the dashed red line corresponds to the right axis.

previous experiments [112,113]. Ag is preferred as a material for plasmonic devices due to its relatively low surface plasmon damping. The Drude model $\epsilon_m(\omega) = \epsilon_\infty - \frac{\omega_p^2}{\omega^2 + i\kappa\omega}$ can be used to describe the dielectric function of the Ag MNP, where the related parameters are the ultraviolet permittivity $\epsilon_\infty = 4.6$ [29], the bulk plasma frequency $\omega_p = 7418.71$ meV (corresponding to the MNP resonance frequency $\omega_m = 2887.73$ meV), and the total decay rate $\kappa = 53.28$ meV, unless otherwise stated. The relevant parameters of the two-level QD are set to be the dipole moment $\mu = 0.7$ e nm, the spontaneous emission decay rate $\gamma = 0.05$ meV, and the dephasing rate $\gamma_{dph} = 0.005$ meV [2,20]. A weak driving field with intensity $I = \epsilon_0 c E_0^2 / 2 = 1$ W/cm² is applied to drive the hybrid MNP-QD system embedded in the vacuum, $\epsilon_b = 1$.

In Eqs. (17) and (18), the relationship between the coupling strength g and the system parameters as well as the relationship between the dipole moment χ and the system parameters is presented. In order to more intuitively depict them, we plot the coupling strength g and the modulus of the complex dipole moment χ of the MNP versus the MNP-QD center-to-center distance d in Fig. 2(a). As shown in Fig. 2(a), the coupling strength g decreases monotonically with the increase of d and diminishes to a small value $g = 1.824$ meV when $d = 24$ nm. Since the dipole moment χ of the MNP is independent of d , the change of $|\chi|$ appears as a straight line that keeps its value constant. Figure 2(b) displays the dependence of the coupling strength g between the MNP and QD and the modulus of the complex dipole moment χ of the MNP on the MNP radius r_m . As can be easily seen from Fig. 2(b), both the coupling strength g and the modulus of complex dipole moment χ of the MNP show a monotonically increasing trend with the increase of the MNP radius r_m , which is apparent because both of them are proportional to the third half power of r_m , $r_m^{3/2}$.

It is worth mentioning that the decay rate κ of the MNP in our model is tens of meV. Referring to Fig. 2(a), it can be seen that the coupling strength g between the MNP and QD changes in a small range from 0 to 10 meV within

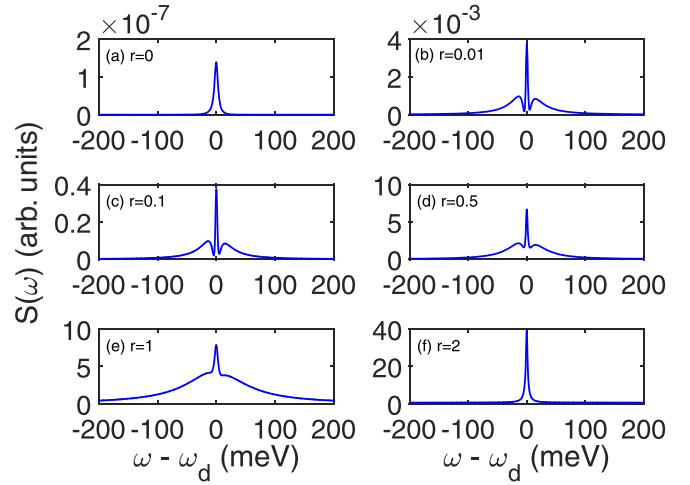


FIG. 3. The fluorescence spectra for $S_\alpha = 2$, $\mu = 0.7$ e nm, $r_m = 7$ nm, $d = 14$ nm, $\epsilon_b = 1$, $\gamma = 0.05$ meV, $\gamma_{dph} = 0.005$ meV, $\phi = 0$, $I = 1$ W/cm², $\Delta_m = 0$ meV, and $\Delta = 0$ meV. Six panels show six different squeezing amplitudes: (a) $r = 0$; (b) $r = 0.01$; (c) $r = 0.1$; (d) $r = 0.5$; (e) $r = 1$; and (f) $r = 2$, respectively.

the achievable parameter range. This means that $g < \kappa/2$, namely, the optical properties of nanoscale plasmon-exciton QED system are studied under the weak-coupling regime of MNP-QD, which makes the actualization of our scheme more experimental friendly.

IV. NUMERICAL RESULTS AND DISCUSSIONS ABOUT THE EMISSION FLUORESCENCE SPECTRA

In this section, we numerically in detail shed light on dynamic optical responses, i.e., resonance fluorescence, of the hybrid system which contains an Ag spherical MNP and a colloidal CdSe QD using experimentally realistic parameters. First, we analyze how the squeezing strength r modifies the emission power spectra. As shown in Fig. 3, the shape of the spectral line depend sensitively upon the value of the squeezing strength r . In the absence of the squeezed vacuum field [i.e., $r = 0$ as shown in Fig. 3(a)], the emission spectrum displays a nearly symmetric Lorentzian-like profile. However, when the squeezed vacuum field is applied, the shape of the spectral line changes obviously even if the squeezing strength r is taken as a small value. We can observe that the emission spectrum presents a three-peaked structure with the central peak having a narrow line in Fig. 3(b). At the same time, the intensity of the emission spectrum increases by more than four orders of magnitude, which implies that the emission spectrum is quite sensitive to the variation of the squeezed vacuum field. Compared with Fig. 3(b), when the squeezing strength r increases from 0.01 to 0.1, the line shape of the three peak distribution does not change, but the intensity of the emission spectrum increases by nearly two orders of magnitude in Fig. 3(c). When the squeezing strength is equal to $r = 0.5$, the emission spectrum presents a nearly symmetrical three-peak distribution, and the position of two dips is elevated as shown in Fig. 3(d). For the case of the squeezing strength $r = 1$, the two peaks on both sides of the central peak in the emission spectrum become less obvious in

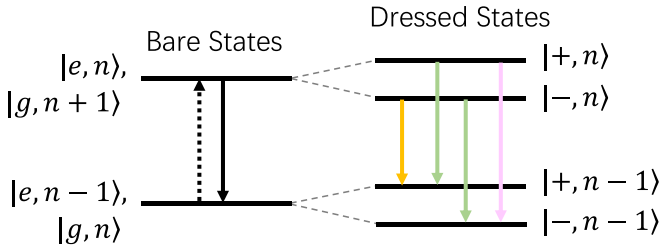


FIG. 4. Schematic illustration of the evolution from the bare-state scenario to the dressed-state picture with three nondegenerate transitions under excitation.

Fig. 3(e). When the squeezing strength increasing to $r = 2$, the emission spectrum exhibits the line shape where the two peaks on both sides disappear and only the central peak with high strength narrow line exists in Fig. 3(f). Throughout the six panels presented in Fig. 3, the overall trend that the intensity of the emission spectra increases with the increase of the squeezing strength r is captured. Thus, it is evident that the squeezing strength can determine the width of the spectral line, the number of the emission peaks, and the peak-value magnitudes of the emission spectrum. Overall, the obtained results show that the introduction of the squeezed vacuum can significantly change the optical fluorescence properties of the hybrid system.

In fact, all interactions, which are relevant for atomic and condensed matter physics, are mediated by quantum fluctuations of the electromagnetic field vacuum. For this reason, the squeezed vacuum (controlling the vacuum fluctuations) can be utilized as a resource for engineering the strength and the range of matter-field interactions. Similarly, acting as a mold, the squeezed vacuum imprints its squeezing feature to our MNP-QD scheme. According to the previous studies in Refs. [89,114], we can conclude qualitatively that the coupling strength g between the MNP plasmonic field mode and the two-level QD significantly increases with the squeezing parameter r . As a consequence, in the presence of the squeezed field, the spectrum of the fluorescence is dramatically altered and the intensity of the fluorescence is considerably enhanced even in the weak-coupling regime of MNP-QD. We have performed extensive numerical calculations, all results support this claim, but it is difficult to prove quantitatively and analytically.

On the other hand, this is a key feature of the dynamic Stark splitting effect (see Fig. 4), which originates from the above-mentioned strong coherent coupling between the MNP plasmonic field mode and the two-level QD. Figure 4 shows the evolution from the bare states to the dressed states for appropriate values of the squeezing parameter (e.g., $0 < r \leq 1$). It is easy to find that in the dressed-state quadruplet there are four radiative transitions, in which two degenerate ones (see green arrow in Fig. 4), namely, three nondegenerate transitions [75]. Together they form the three-peaked emission: a central peak and two sidebands at moderate squeezing values as displayed in Figs. 3(b)–3(e). Yet it is worth pointing out that, for sufficiently strong squeezing as shown in Fig. 3(f), this well-behaved structure is completely destroyed. Specifically, the central peak is drastically raised whereas the original

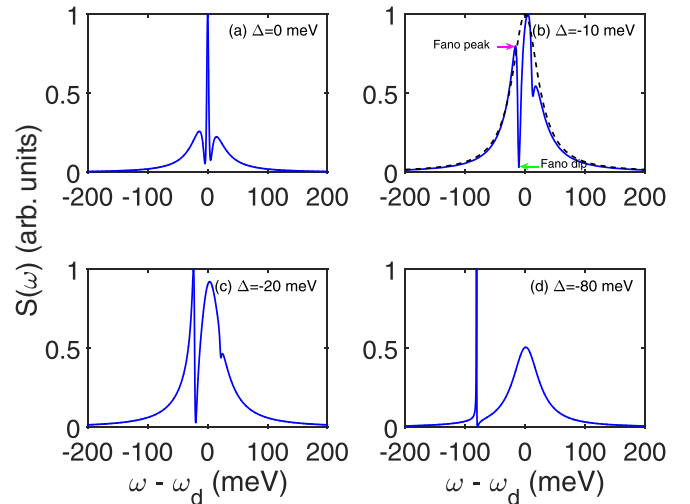


FIG. 5. The normalized fluorescence spectra for $S_\alpha = 2$, $\mu = 0.7$ e nm, $r_m = 7$ nm, $d = 14$ nm, $\epsilon_b = 1$, $\gamma = 0.05$ meV, $\gamma_{dph} = 0.005$ meV, $r = 0.1$, $\phi = 0$, $\Delta_m = 0$ meV, and $I = 1$ W/cm². Four panels show four different frequency detunings between the plasmon resonance frequency of the MNP and the exciton resonance frequency of the QD: (a) $\Delta = 0$ meV; (b) $\Delta = -10$ meV; (c) $\Delta = -20$ meV; and (d) $\Delta = -80$ meV, respectively.

two sidebands are slowly increased and are too small to be emerged with respect to the central peak in the large squeezing limit. So a typical single-peaked line shape is generated in the fluorescence spectrum.

In the analysis above, we consider the resonant case for the two frequencies of the MNP (ω_m) and the QD exciton (ω_x): $\omega_m = \omega_x$, namely, $\Delta = 0$. However, for the exciton resonance frequency (ω_x) of the two-level QD (such as a CdSe QD) far below the plasmon resonance frequency ω_m of the MNP (such as an Ag MNP) due to the QD size, it is worth exploring the situation where the MNP and QD are not resonant, i.e., $\Delta \neq 0$. In view of this, we consider the impact of the frequency detuning Δ between the plasmon resonance frequency of the MNP and the exciton resonance frequency of the QD on the emission spectra $S(\omega)$. As shown in Fig. 5(a), when the QD resonates with the MNP, we can find that there are three peaks, of which the peaks on both sides have normal width, while the peak in the middle has narrow width. In order to clarify the role of the QD, the black dashed line in Fig. 5(b) depicts the emission spectrum without the QD as a comparison. In Fig. 5(b) we can clearly see that a symmetric Lorentzian profile exists in the emission spectrum in the absence of the QD [see black dashed line in Fig. 5(b)]. However, in the presence of QD, quantum interference between two competing optical pathways can arouse the occurrence of the Fano-type resonance fluorescence, from a physical point of view. Specifically, the basic excitations in MNP are surface plasmons with quasicontinuous spectrum (i.e., a broad response line), while the excitons in QD are discrete interband excitons (i.e., a sharp response line). When the exciton energy is near the plasmon peak, the coupling effect between the exciton and plasmon is enhanced, and the Fano interference between the quasicontinuous excitation of MNP and the discrete excitation of QD, where these two responses overlap, leads to the asymmetric

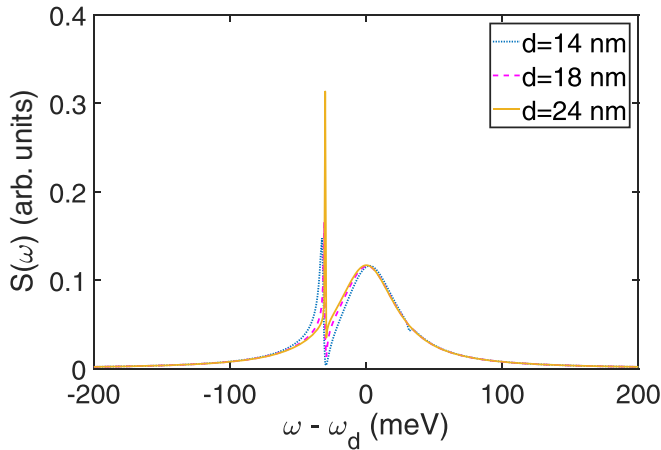


FIG. 6. The fluorescence spectra as a function of the frequency ω for the three different MNP-to-QD distances $d = 14$ nm (blue dotted line), $d = 18$ nm (magenta dashed line), and $d = 24$ nm (yellow solid line). The other parameters used here are $S_\alpha = 2$, $\mu = 0.7$ e nm, $r_m = 7$ nm, $\epsilon_b = 1$, $\gamma = 0.05$ meV, $\gamma_{dph} = 0.005$ meV, $r = 0.1$, $\phi = 0$, $I = 1$ W/cm², $\Delta_m = 0$ meV, and $\Delta = -30$ meV, respectively.

Fano line shape. The squeezing can enhance this effect. In Fig. 5(b) the whole emission spectrum splits into three peaks and the emission spectrum is highly suppressed for particular frequency (near the resonance frequency of the QD). The fluorescence dip resulting from the high suppression is regarded as Fano dip [see the green arrow in Fig. 5(b)]. While, in the case of slightly lower energy, the enhancement of the emission spectrum caused by the constructive interference can be observed [see blue solid line in Fig. 5(b)]. The fluorescence peak caused by the high enhancement is called Fano peak [see the magenta arrow in Fig. 5(b)]. When the frequency detuning $\Delta = -20$ meV, the height of the left peak exceeds the central peak, and the smaller peak on the right becomes less obvious in Fig. 5(c). When further increasing the frequency detuning to $\Delta = -80$ meV, the left peak evolves into an ultranarrow line with the enhanced height, and there is a fluorescence quenching point near the resonance frequency of the QD in Fig. 5(d). The peak on the right almost disappears, and the curve on the right tends to be smooth. Meanwhile, the location of the left two peaks moves away from each other, and the linewidth on the right widens, visibly to the naked eye. According to what has been analyzed above, we can reach the conclusion that the frequency detuning between the resonance frequency of the MNP and the resonance frequency of the QD has an obvious impact on the spectral line shape, the spectral line width, and the number of the emission peaks in the hybrid MNP-QD system.

Subsequently, we look into the modification of the emission spectra by suitably varying the center-to-center distance d between the MNP and QD. From the previous information given in Fig. 2(a), it can be concluded that the coupling strength g between the MNP and QD decreases with the continuous separation of the MNP and QD, while the dipole moment χ of the MNP is not affected by d . For the convenience of comparison, we plot the emission spectra with the frequency ω as the variable under the three different d as shown in Fig. 6. Here $d = 14$ nm (blue dotted line),

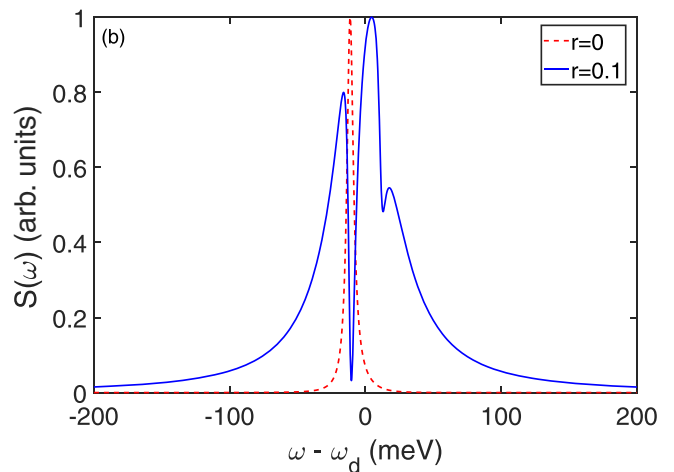
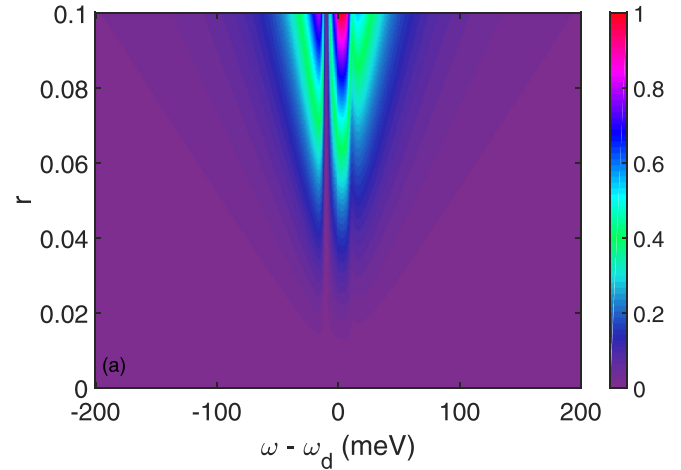


FIG. 7. (a) Two-dimensional plot for the normalized fluorescence spectra as a function of the squeezing strength r and the frequency ω . (b) The normalized fluorescence spectra as a function of the frequency ω for the two different squeezing strength $r = 0$ (red dashed line) and $r = 0.1$ (blue solid line). Lines are normalized by the maximum peak value of each line. The other system parameters have been set to $S_\alpha = 2$, $\mu = 0.7$ e nm, $r_m = 7$ nm, $d = 14$ nm, $\epsilon_b = 1$, $\gamma = 0.05$ meV, $\gamma_{dph} = 0.005$ meV, $\phi = 0$, $I = 1$ W/cm², $\Delta_m = 0$ meV, and $\Delta = -10$ meV, respectively.

$d = 18$ nm (magenta dashed line), and $d = 24$ nm (yellow solid line) correspond to $g = 9.189$ meV, $g = 4.324$ meV, and $g = 1.824$ meV, respectively. When $d = 14$ nm (see blue dotted line in Fig. 6), the spectrum shows an asymmetric Fano line shape. With the increase of the distance d , the left resonance peak blue shifts slightly and gradually evolves into an ultranarrow peak along with the increase of its height. The height of the peak on the right is basically unchanged, but the position of the right peak red shifts slightly. The position of the Fano dip is gradually elevated, which indicates that the destructive interference between the MNP and QD weakens with the increasing of the distance d .

Figure 7(a) displays a color-scale two-dimensional map of the emission spectra against the squeezing strength r and the frequency ω . In Fig. 7(a), a dark purple line (near $\omega - \omega_d = -10$ meV) across the spectrum indicates that the emission

spectra are strongly suppressed at these positions. While the bright colored areas (shown in red, magenta, blue, cyan, and green) on both sides of the dark purple line show that the emission spectra are strongly enhanced in these areas. In order to reveal the role of the squeezed vacuum more conveniently, we plot the emission spectra $S(\omega)$ as a function of the frequency ω for the two different squeezing strength [selected from Fig. 7(a)] $r = 0$ (red dashed line) and $r = 0.1$ (blue solid line) in Fig. 7(b). As shown in Fig. 7(b), the emission spectrum displays a Lorentzian-like profile in the absence of the squeezed vacuum field ($r = 0$, see red dashed line). Whereas in the presence of the squeezed vacuum field [i.e., $r = 0.1$, see blue solid line in Fig. 7(b)], the Fano resonance effect occurs, which is manifested as the emission spectrum splitting into three peaks. When the squeezing strength $r = 0.1$, the Fano dip with strong suppression appears at the position where the peak appears in the case of $r = 0$. And the Fano peak with strong enhancement emerges at the left shoulder of the Fano dip. Interestingly, we can see an additional shallow Fano profile at the right shoulder.

The key features contained in Figs. 7(a) and 7(b) are summarized in the following: (1) with the increase of the squeezing strength, the peak-value magnitudes of the spectral line also increase; (2) in the presence of the squeezed vacuum, the hybrid MNP-QD system can support the Fano-type resonance fluorescence, which has strong spectral enhancement and suppression in a wide range owing to the constructive and destructive interference. The above results signify that some interesting phenomena can be obtained in the rich spectral responses due to the introduction of the squeezed vacuum, e.g., sharp asymmetric fluorescence, fluorescence enhancement, and fluorescence suppression. In addition, we can design and control the peak-value magnitudes of the resonance fluorescence spectra under the influence of the squeezed vacuum.

Next, in order to further explore the effect of the MNP radius r_m on the emission spectra $S(\omega)$, we also plot the emission spectra $S(\omega)$ versus the frequency ω for the four different r_m in Fig. 8. As described in Eqs. (17) and (18), the coupling strength g between the MNP and QD and the dipole moment χ of the MNP are strongly dependent on the MNP radius r_m , as shown by the fact that they are both proportional to the third half power of r_m . Here we increase r_m from 1 nm to 7 nm every 2 nm with a fixed $d = 14$ nm, accompanied by the constant increase of g and χ . It can be clearly seen from Fig. 8(a) that only an ultranarrow spectral line exists in the emission spectrum when $r_m = 1$ nm. At this time, the interaction between the MNP and QD is very weak (i.e., $g = 0.6753$ meV) and the dipole moment of the MNP is very small (i.e., $|\chi| = 0.4962$ e nm), which leads to only an ultranarrow line near the QD resonance frequency in the emission spectrum. As the MNP radius increases to $r_m = 3$ nm, the right peak with the MNP resonance frequency as the center frequency begins to appear. An asymmetric Fano profile emerges in the emission spectrum in Fig. 8(b). With the further increase of the MNP radius r_m , the height of the right peak is enhanced obviously due to the increase of the coupling strength g between the MNP and QD and the dipole moment χ of the MNP. And the width of the left spectral line is slightly wider in Fig. 8(c). When the MNP radius $r_m = 7$ nm, the left peak width becomes wider, the height of

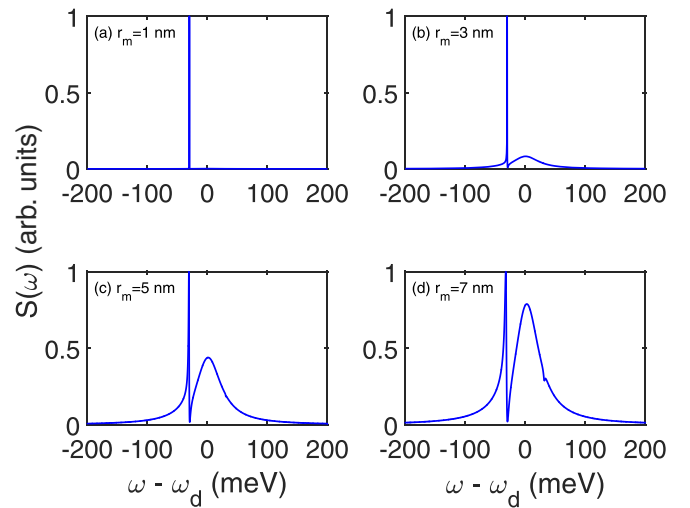


FIG. 8. The normalized fluorescence spectra for $S_\alpha = 2$, $\mu = 0.7$ e nm, $d = 14$ nm, $\epsilon_b = 1$, $\gamma = 0.05$ meV, $\gamma_{dph} = 0.005$ meV, $r = 0.1$, $\phi = 0$, $I = 1$ W/cm², $\Delta_m = 0$ meV, and $\Delta = -30$ meV. Four panels show four different MNP radius: (a) $r_m = 1$ nm; (b) $r_m = 3$ nm; (c) $r_m = 5$ nm; and (d) $r_m = 7$ nm, respectively.

the central peak increases significantly, and an insignificant small peak appears on the right side in Fig. 8(d). From the analysis above, we find that tuning the MNP radius r_m , thus changing the magnitude of the coupling strength between the MNP and QD and the dipole moment of the MNP [see Eqs. (17) and (18)], can tailor and control the line shape of the emission spectrum, which determines both the width of the spectrum line and the number of the emission peaks.

Finally, we discuss the effect of the orientation of the external applied field on the emission spectrum. We previously investigate the situation where the polarization of the incident field is along the major axis of the hybrid MNP-QD system

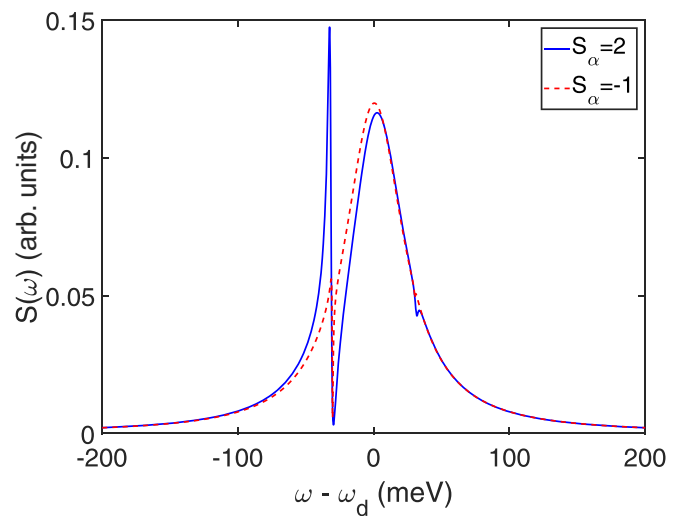


FIG. 9. The fluorescence spectra for $\mu = 0.7$ e nm, $r_m = 7$ nm, $d = 14$ nm, $\epsilon_b = 1$, $\gamma = 0.05$ meV, $\gamma_{dph} = 0.005$ meV, $r = 0.1$, $\phi = 0$, $I = 1$ W/cm², $\Delta_m = 0$ meV, and $\Delta = -30$ meV. For comparison, we consider the two different orientation parameters: $S_\alpha = 2$ (blue solid line) and $S_\alpha = -1$ (red dashed line), respectively.

(cf. Fig. 1), i.e., $S_\alpha = 2$. Now we turn to the scenario where the polarization of the incident field is orthogonal to the major axis of the MNP-QD system, i.e., $S_\alpha = -1$. When $S_\alpha = 2$, the spectral line manifests an obvious Fano resonance line-shape profile with high spectral enhancement and suppression (blue solid line in Fig. 9). Nevertheless, compared with the case of $S_\alpha = 2$, the spectral suppression occurs at the same position in both cases, but the degree of the spectral enhancement is inhibited for the case of $S_\alpha = -1$ (red dashed line in Fig. 9). The effect of Fano interference is weakened, resulting in a significantly reduced enhancement of the emission spectrum. This indicates that the polarization direction of the external applied field can be used to engineer the fluorescence spectrum of the hybrid MNP-QD system.

V. CONCLUSIONS

In summary, we have demonstrated the feasibility of utilizing quantum squeezed reservoir to engineer and control the optical fluorescence spectra of the MNP-QD molecule by applying an external driving field. Based on the quantum master-equation approach and experimentally achievable parameters for the MNP-QD QED system, our obtained in-depth results indicate that some desired spectral features such as sharp asymmetric Fano-type resonance fluorescence, fluorescence quenching, fluorescence narrowing, and fluorescence enhancement can be caught in the emission spectra by appropriately modulating the squeezing parameter, the frequency detuning between the MNP and QD, the center-to-center distance between the MNP and QD, the MNP radius, and the polarization direction of the external applied field. Besides, in this way we show that the number of the fluorescence peaks as well as the positions of the fluorescence quenching can be also adjusted. Alternatively, these optical properties of the hybrid system achieved here can work in the weak-coupling regime of MNP-QD, which makes the implementation of this proposal more experimental friendly. The tunability of the fluorescence spectra ensures the potential availability of the flexible ultracompact hybrid MNP-QD system in related applications, such as sensing, lasing, switching, and optical modulator. We hope that our results could stimulate experimental implementations on Fano-type resonance fluorescence with a squeezed vacuum.

ACKNOWLEDGMENTS

We acknowledge the anonymous referees for their valuable and insightful suggestions. We would also like to thank Rong Yu and Xiaoxue Yang for enlightening discussions. In the present research, S.S., Z.W., and J.L. were supported in part by the National Key Research and Development Program of China under Contract No. 2016YFA0301200, by the National Natural Science Foundation of China through Grant No. 11675058, and by the Fundamental Research Funds for the Central Universities, Huazhong University of Science and Technology (HUST), under Project No. 2018KFYYXJJ037. Y.W. was supported partially by the National Natural Science Foundation of China through Grants No. 11875029 and No. 11574104.

APPENDIX A: DERIVATION OF THE SURFACE PLASMON RESONANCE FREQUENCY ω_m OF THE MNP

In this Appendix we provide details about the formula for the surface plasmon resonance frequency ω_m of the MNP. When the size of the spherical MNP is much smaller than the wavelength of incident light ($r_m \ll \lambda$), the quasistatic approximation can be used to solve the scattering problem of the MNP. Due to the small size of nanostructures, we assume that the applied driving field is spatially uniform, which means that the phase of the driving field at any given time is approximately the same in the whole volume of the MNP. The dipole approximation can be used to describe the properties of the single MNP effectively and conveniently. Besides, it is well known that the dielectric under the external field driving can induce additional electric field due to the polarization, and the enhancement factor of the electric field is proportional to the polarizability α . In this case, the polarizability of the MNP in the electrostatic field can be used to represent its polarizability in the incident electric field. Therefore, the polarizability of the MNP can be expressed as [115]

$$\alpha = 4\pi r_m^3 \frac{\epsilon_m(\omega) - \epsilon_b}{\epsilon_m(\omega) + 2\epsilon_b}, \quad (\text{A1})$$

where r_m is the radius of the MNP, ϵ_b is the dielectric constant of the environment where the hybrid MNP-QD system is embedded, and the dielectric function of the MNP can be given by the Drude model

$$\epsilon_m(\omega) = \epsilon_\infty - \frac{\omega_p^2}{\omega^2 + i\kappa\omega}; \quad (\text{A2})$$

here ϵ_∞ is the ultraviolet permittivity of silver, ω_p is the plasma frequency, and κ is the damping rate of silver, respectively. For general media, the above expression (A1) has nothing special, but it can display a very interesting phenomenon for the surface plasmons, which is completely based on the fact that the real part of the dielectric function of the surface plasmon is negative [4]. Mathematically, the point where the polarizability α of the MNP reaches an infinity value corresponds to the denominator of Eq. (A1) close to zero, which means that $|\epsilon_m(\omega) + 2\epsilon_b|$ approaching to zero is required. Physically, the so-called LSPR occurs when the polarization of the MNP α is large, which is also the reason for the field amplification both inside and near the MNP. In addition, the materials exhibit good plasmonic properties if the two conditions (1) $\text{Re}[\epsilon_m(\omega)] < 0$ and (2) $\text{Im}[\epsilon_m(\omega)] \ll -\text{Re}[\epsilon_m(\omega)]$ are satisfied simultaneously [3,4], where $\text{Re}[\cdot]$ denotes the real part of the magnitude enclosed in square brackets and $\text{Im}[\cdot]$ the imaginary part. Note that the above-mentioned conditions are valid, e.g., for silver in the most of the visible region. In this scenario, the requirement of the LSPR can be simplified as the Fröhlich condition [1]

$$\text{Re}[\epsilon_m(\omega)] = -2\epsilon_b. \quad (\text{A3})$$

Based on the above analysis, it is reasonable to give the expression of the surface plasmon resonance frequency of the MNP

$$\omega_m \approx \frac{\omega_p}{\sqrt{2\epsilon_b + \epsilon_\infty}}, \quad (\text{A4})$$

as claimed in the main text.

APPENDIX B: DERIVATION OF THE FORMULAS (17) AND (18)

When the hybrid system is excited by an external electric field polarized along the system axis joining the MNP and QD structure, the oscillating electric field felt by the MNP is a superposition of the input field E_{dri} and the dipole response field E_{QD} of the QD. In the electrostatic approach, according to the Laplace equation for the electric potential $\nabla^2\Phi = 0$, the electric potential Φ can be obtained by using the boundary conditions. And the expression of the electric field can be further calculated according to the formula $E = -\nabla\Phi$, with the forms

$$E_{\text{ins}} = \frac{3\epsilon_b}{\epsilon_m(\omega) + 2\epsilon_b} E_{\text{in}}, \quad (\text{B1})$$

$$E_{\text{out}} = E_{\text{in}} + E_m, \quad (\text{B2})$$

where E_{ins} and E_{out} represent the electric fields inside and outside the MNP sphere, respectively. Above, E_{in} contains the external input field E_{dri} and the dipole response field E_{QD} generated by the QD, which has the form of $E_{\text{in}} = E_{\text{dri}} + E_{\text{QD}}$. In the case that the radius of the MNP sphere is far less than the wavelength of the incident plane wave ($r_m \ll \lambda$), it is effective to represent the MNP as the ideal dipole in the quasistatic region [1,116]. Therefore, the electric field E_m generated by the MNP outside the sphere can be expressed as

$$E_m = \frac{S_\alpha P_{\text{MNP}}}{4\pi\epsilon_0\epsilon_b d^3}, \quad (\text{B3})$$

where S_α is the orientation parameter set to 2 (or -1) if the external driving field E_{dri} is polarized along (or perpendicular to) the major axis of the hybrid MNP-QD system. ϵ_0 and ϵ_b are the vacuum dielectric constant and the relative dielectric constant of the background medium, respectively. d is the center-to-center distance between the MNP and QD. P_{MNP} is the dipole moment of the MNP, which can be written as

$$P_{\text{MNP}} = 4\pi\epsilon_0\epsilon_b\beta r_m^3 E_{\text{in}}. \quad (\text{B4})$$

If we consider only the positive frequency part of the dipole moment of the MNP, it has the following form:

$$P_{\text{MNP}}^+ = 4\pi\epsilon_0\epsilon_b\beta r_m^3 \left(E_0 + \frac{S_\alpha P_{\text{QD}}^\dagger}{4\pi\epsilon_0\epsilon_b d^3} \right), \quad (\text{B5})$$

where β is the Clausius Mossotti factor of the MNP, indicated by

$$\beta = \frac{\epsilon_m(\omega) - \epsilon_b}{\epsilon_m(\omega) + 2\epsilon_b}. \quad (\text{B6})$$

According to the expression of the dielectric function of the MNP $\epsilon_m(\omega) = \epsilon_\infty - \frac{\omega_p^2}{\omega^2 + i\kappa\omega}$ given in Eq. (A2), we carry out the first-order Taylor expansion of $\text{Re}[\epsilon_m(\omega)]$ around ω_m and utilize the Fröhlich condition in Eq. (A3) to obtain [2]

$$\beta \cong \frac{3i\epsilon_b\eta}{i(\omega_m - \omega) + \frac{\kappa}{2}}, \quad (\text{B7})$$

where the parameter η is yielded by the formula $\eta = \left\{ \frac{d\text{Re}[\epsilon_m(\omega)]}{d\omega} \Big|_{\omega=\omega_m} \right\}^{-1} = \frac{[\omega_p^2 + \kappa^2(2\epsilon_b + \epsilon_\infty)]^2}{2(2\epsilon_b + \epsilon_\infty)^{\frac{3}{2}}\omega_p^3}$ and the decay rate of the MNP is contributed by $\kappa = 2\eta\text{Im}[\epsilon_m(\omega_m)]$.

When we substitute Eq. (B7) into Eq. (B4) and further substitute the obtained result into Eq. (B3), then consider only the part where the electric field oscillates with $e^{-i\omega t}$, we can get the classical expression for the positive frequency part of the electric field generated by the MNP:

$$E_m^+ = \frac{3i\epsilon_b\eta S_\alpha r_m^3}{(i\Delta_m + \frac{\kappa}{2})d^3} \left(E_0 + \frac{S_\alpha P_{\text{QD}}^\dagger}{4\pi\epsilon_0\epsilon_b d^3} \right). \quad (\text{B8})$$

The expectation value of the dipole response field generated by the surface plasmon of the MNP can be obtained by using the master equation, whose positive frequency component is

$$\langle E_m^+ \rangle = i\varepsilon \langle a \rangle = \frac{i\hbar g^2 \langle \sigma \rangle}{\mu(i\Delta_m + \frac{\kappa}{2})} + \frac{-g\chi E_0}{\mu(i\Delta_m + \frac{\kappa}{2})}. \quad (\text{B9})$$

Comparing the expectation value of the MNP electric field [Eq. (B9)] in the quantum form with the surface plasmon field produced by the MNP [Eq. (B8)] felt by the QD in the classical form, and considering only the positive frequency coefficient, we can arrive at

$$g = \frac{S_\alpha \mu}{d^3} \sqrt{\frac{3r_m^3 \eta}{4\pi\epsilon_0 \hbar}}, \quad (\text{B10})$$

$$\chi = -i\epsilon_b \sqrt{12\eta\epsilon_0\pi\hbar r_m^3}, \quad (\text{B11})$$

i.e., Eqs. (17) and (18). Due to the relationship $\hbar g = \mu\varepsilon$ [3], we can naturally give the expression for $\varepsilon = \frac{\hbar g}{\mu} = \frac{\hbar S_\alpha}{d^3} \sqrt{\frac{3r_m^3 \eta}{4\pi\epsilon_0 \hbar}}$. In addition, we can get a more in-depth result by directly comparing Eq. (B5) with Eq. (15), i.e., $P_{\text{MNP}}^+ = \chi^* \langle a \rangle$.

[1] S. A. Maier, *Plasmonics: Fundamentals and Applications* (Springer Science and Business Media, New York, 2007).
 [2] A. Ridolfo, O. Di Stefano, N. Fina, R. Saija, and S. Savasta, Quantum Plasmonics with Quantum Dot-Metal Nanoparticle Molecules: Influence of the Fano Effect on Photon Statistics, *Phys. Rev. Lett.* **105**, 263601 (2010).
 [3] H. Hapuarachchi, M. Premaratne, Q. L. Bao, W. L. Cheng, S. D. Gunapala, and G. P. Agrawal, Cavity QED analysis of an exciton-plasmon hybrid molecule via the generalized nonlocal optical response method, *Phys. Rev. B* **95**, 245419 (2017).

[4] M. I. Stockman, Nanoplasmonics: Past, present, and glimpse into future, *Opt. Express* **19**, 22029 (2011).
 [5] W. L. Barnes, A. Dereux, and T. W. Ebbesen, Surface plasmon subwavelength optics, *Nature (London)* **424**, 824 (2003).
 [6] P. Peng, Y. C. Liu, D. Xu, Q. T. Cao, G. Lu, Q. Gong, and Y. F. Xiao, Enhancing Coherent Light-Matter Interactions Through Microcavity-Engineered Plasmonic Resonances, *Phys. Rev. Lett.* **119**, 233901 (2017).
 [7] M. A. Noginov, G. Zhu, A. M. Belgrave, R. Bakker, V. M. Shalaev, E. E. Narimanov, S. Stout, E. Herz, T. Suteewong,

- and U. Wiesner, Demonstration of a spaser-based nanolaser, *Nature (London)* **460**, 1110 (2009).
- [8] D. X. Zhao, Y. Gu, H. Y. Chen, J. J. Ren, T. C. Zhang, and Q. H. Gong, Quantum statistics control with a plasmonic nanocavity: Multimode-enhanced interferences, *Phys. Rev. A* **92**, 033836 (2015).
- [9] K. R. McEnery, M. S. Tame, S. A. Maier, and M. S. Kim, Tunable negative permeability in a quantum plasmonic metamaterial, *Phys. Rev. A* **89**, 013822 (2014).
- [10] S. Savasta, R. Saija, A. Ridolfo, O. Di Stefano, P. Denti, and F. Borghese, Nanopolaritons: Vacuum Rabi splitting with a single quantum dot in the center of a dimer nanoantenna, *ACS Nano* **4**, 6369 (2010).
- [11] M. S. Tame, K. R. McEnery, S. K. Özdemir, J. Lee, S. A. Maier, and M. S. Kim, Quantum plasmonics, *Nat. Phys.* **9**, 329 (2013).
- [12] M. T. Cheng, S. D. Liu, H. J. Zhou, Z. H. Hao, and Q. Q. Wang, Coherent exciton-plasmon interaction in the hybrid semiconductor quantum dot and metal nanoparticle complex, *Opt. Lett.* **32**, 2125 (2007).
- [13] J. Y. Yan, W. Zhang, S. Duan, X. G. Zhao, and A. O. Govorov, Optical properties of coupled metal-semiconductor and metal-molecule nanocrystal complexes: Role of multipole effects, *Phys. Rev. B* **77**, 165301 (2008).
- [14] A. M. Kelley, A molecular spectroscopic description of optical spectra of J-aggregated dyes on gold nanoparticles, *Nano Lett.* **7**, 3235 (2007).
- [15] R. D. Artuso and G. W. Bryant, Optical response of strongly coupled quantum dot-metal nanoparticle systems: Double peaked Fano structure and bistability, *Nano Lett.* **8**, 2106 (2008).
- [16] S. Nie and S. R. Emory, Probing single molecules and single nanoparticles by surface-enhanced Raman scattering, *Science* **275**, 1102 (1997).
- [17] K. Kneipp, Y. Wang, H. Kneipp, L. T. Perelman, I. Itzkan, R. R. Dasari, and M. S. Feld, Single Molecule Detection Using Surface-Enhanced Raman Scattering (SERS), *Phys. Rev. Lett.* **78**, 1667 (1997).
- [18] J. N. Anker, W. P. Hall, O. Lyandres, N. C. Shah, J. Zhao, and R. P. Van Duyne, Biosensing with plasmonic nanosensors, *Nat. Mater.* **7**, 442 (2008).
- [19] E. Waks and D. Sridharan, Cavity QED treatment of interactions between a metal nanoparticle and a dipole emitter, *Phys. Rev. A* **82**, 043845 (2010).
- [20] W. Zhang, A. O. Govorov, and G. W. Bryant, Semiconductor-Metal Nanoparticle Molecules: Hybrid Excitons and the Nonlinear Fano Effect, *Phys. Rev. Lett.* **97**, 146804 (2006).
- [21] W. Zhang and A. O. Govorov, Quantum theory of the nonlinear Fano effect in hybrid metal-semiconductor nanostructures: The case of strong nonlinearity, *Phys. Rev. B* **84**, 081405(R) (2011).
- [22] R. A. Shah, N. F. Scherer, M. Pelton, and S. K. Gray, Ultrafast reversal of a Fano resonance in a plasmon-exciton system, *Phys. Rev. B* **88**, 075411 (2013).
- [23] P. Anger, P. Bharadwaj, and L. Novotny, Enhancement and Quenching of Single-Molecule Fluorescence, *Phys. Rev. Lett.* **96**, 113002 (2006).
- [24] K. T. Shimizu, W. K. Woo, B. R. Fisher, H. J. Eisler, and M. G. Bawendi, Surface-Enhanced Emission from Single Semiconductor Nanocrystals, *Phys. Rev. Lett.* **89**, 117401 (2002).
- [25] C. R. Simovski, M. S. M. Mollaei, and P. M. Voroshilov, Fluorescence quenching by plasmonic nanoantennas, *Phys. Rev. B* **101**, 245421 (2020).
- [26] A. Mohammadzadeh and M. Miri, Resonance fluorescence of a hybrid semiconductor-quantum-dot-metalnanoparticle system driven by a bichromatic field, *Phys. Rev. B* **99**, 115440 (2019).
- [27] F. Carreño, M. A. Antón, V. Yannopapas, and E. Paspalakis, Control of resonance fluorescence of a four-level quantum emitter near a plasmonic nanostructure, *Phys. Rev. A* **95**, 043825 (2017).
- [28] C. Van Vlack, P. T. Kristensen, and S. Hughes, Spontaneous emission spectra and quantum light-matter interactions from a strongly coupled quantum dot metalnanoparticle system, *Phys. Rev. B* **85**, 075303 (2012).
- [29] A. Delga, J. Feist, J. Bravo-Abad, and F. J. García-Vidal, Quantum Emitters Near a Metal Nanoparticle: Strong Coupling and Quenching, *Phys. Rev. Lett.* **112**, 253601 (2014).
- [30] T. Pons, I. L. Medintz, K. E. Sapsford, S. Higashiya, A. F. Grimes, D. S. English, and H. Mattoussi, On the quenching of semiconductor quantum dot photoluminescence by proximal gold nanoparticles, *Nano Lett.* **7**, 3157 (2007).
- [31] V. Yannopapas, E. Paspalakis, and N. V. Vitanov, Plasmon-Induced Enhancement of Quantum Interference Near Metallic Nanostructures, *Phys. Rev. Lett.* **103**, 063602 (2009).
- [32] T. S. Theuerholz, A. Carmele, M. Richter, and A. Knorr, Influence of Förster interaction on light emission statistics in hybrid systems, *Phys. Rev. B* **87**, 245313 (2013).
- [33] R. Sáez-Blázquez, J. Feist, A. I. Fernández-Domínguez, and F. J. García-Vidal, Enhancing photon correlations through plasmonic strong coupling, *Optica* **4**, 1363 (2017).
- [34] R. Sáez-Blázquez, J. Feist, F. J. García-Vidal, and A. I. Fernández-Domínguez, Photon statistics in collective strong coupling: Nanocavities and microcavities, *Phys. Rev. A* **98**, 013839 (2018).
- [35] V. G. Bordo, Quantum light from a metal nanoparticle, *Phys. Rev. A* **100**, 063807 (2019).
- [36] F. Carreño, V. Yannopapas, M. A. Antón, and E. Paspalakis, Photon statistics of a quantum emitter close to a lattice of plasmonic nanoparticles, *Phys. Rev. A* **100**, 023802 (2019).
- [37] T. J. Arruda, R. Bachelard, J. Weiner, S. Slama, and P. W. Courteille, Controlling photon bunching and antibunching of two quantum emitters near a core-shell sphere, *Phys. Rev. A* **101**, 023828 (2020).
- [38] X. W. Chen, V. Sandoghdar, and M. Agio, Coherent Interaction of Light With a Metallic Structure Coupled to a Single Quantum Emitter: From Superabsorption to Cloaking, *Phys. Rev. Lett.* **110**, 153605 (2013).
- [39] D. Martín-Cano, H. R. Haakh, K. Murr, and M. Agio, Large Suppression of Quantum Fluctuations of Light from a Single Emitter by an Optical Nanostructure, *Phys. Rev. Lett.* **113**, 263605 (2014).
- [40] M. A. Antón, S. Maede-Razavi, F. Carreño, I. Thanopoulos, and E. Paspalakis, Optical and microwave control of resonance fluorescence and squeezing spectra in a polar molecule, *Phys. Rev. A* **96**, 063812 (2017).
- [41] J. F. Li, Y. F. Huang, Y. Ding, Z. L. Yang, S. B. Li, X. S. Zhou, F. R. Fan, W. Zhang, Z. Y. Zhou, D. Y. Wu, B. Ren, Z. L. Wang, and Z. Q. Tian, Shell-isolated nanoparticle-enhanced Raman spectroscopy, *Nature (London)* **464**, 392 (2010).

- [42] J. Homola, S. S. Yee, and G. Gauglitz, Surface plasmon resonance sensors: Review, *Sens. Actuator B–Chem.* **54**, 3 (1999).
- [43] K. E. Dorfman, P. K. Jha, D. V. Voronine, P. Genevet, F. Capasso, and M. O. Scully, Quantum-Coherence-Enhanced Surface Plasmon Amplification by Stimulated Emission of Radiation, *Phys. Rev. Lett.* **111**, 043601 (2013).
- [44] D. J. Bergman and M. I. Stockman, Surface Plasmon Amplification by Stimulated Emission of Radiation: Quantum Generation of Coherent Surface Plasmons in Nanosystems, *Phys. Rev. Lett.* **90**, 027402 (2003).
- [45] E. Ozbay, Plasmonics: Merging photonics and electronics at nanoscale dimensions, *Science* **311**, 189 (2006).
- [46] N. Engheta, Circuits with light at nanoscales: Optical nanocircuits inspired by metamaterials, *Science* **317**, 1698 (2007).
- [47] D. E. Chang, A. S. Sørensen, E. A. Demler, and M. D. Lukin, A single-photon transistor using nanoscale surface plasmons, *Nat. Phys.* **3**, 807 (2007).
- [48] T. Wijesinghe, M. Premaratne, and G. P. Agrawal, Electrically pumped hybrid plasmonic waveguide, *Opt. Express* **22**, 2681 (2014).
- [49] K. C. Huang, M. K. Seo, T. Sarmiento, Y. J. Huo, J. S. Harris, and M. L. Brongersma, Electrically driven subwavelength optical nanocircuits, *Nat. Photon.* **8**, 244 (2014).
- [50] R. Filter, K. Słowik, J. Straubel, F. Lederer, and C. Rockstuhl, Nanoantennas for ultrabright single photon sources, *Opt. Lett.* **39**, 1246 (2014).
- [51] A. Faraon, I. Fushman, D. Englund, N. Stoltz, P. Petroff, and J. Vučković, Coherent generation of non-classical light on a chip via photon-induced tunnelling and blockade, *Nat. Phys.* **4**, 859 (2008).
- [52] K. M. Birnbaum, A. Boca, R. Miller, A. D. Boozer, T. E. Northup, and H. J. Kimble, Photon blockade in an optical cavity with one trapped atom, *Nature (London)* **436**, 87 (2005).
- [53] T. Peyronel, O. Firstenberg, Q. Y. Liang, S. Hofferberth, A. V. Gorshkov, T. Pohl, M. D. Lukin, and V. Vuletić, Quantum nonlinear optics with single photons enabled by strongly interacting atoms, *Nature (London)* **488**, 57 (2012).
- [54] K. Müller, A. Rundquist, K. A. Fischer, T. Sarmiento, and K. G. Lagoudakis, Coherent Generation of Nonclassical Light on Chip Via Detuned Photon Blockade, *Phys. Rev. Lett.* **114**, 233601 (2015).
- [55] T. C. H. Liew and V. Savona, Single Photons from Coupled Quantum Modes, *Phys. Rev. Lett.* **104**, 183601 (2010).
- [56] M. Bamba, A. Imamoğlu, I. Carusotto, and C. Ciuti, Origin of strong photon antibunching in weakly nonlinear photonic molecules, *Phys. Rev. A* **83**, 021802(R) (2011).
- [57] A. D. Yoffe, Semiconductor quantum dots and related systems: Electronic, optical, luminescence and related properties of low dimensional systems, *Adv. Phys.* **50**, 1 (2001).
- [58] W. Rechberger, A. Hohenau, A. Leitner, J. R. Krenn, B. Lamprecht, and F. R. Aussenegg, Optical properties of two interacting gold nanoparticles, *Opt. Commun.* **220**, 137 (2003).
- [59] U. Hohenester and A. Trügler, Interaction of single molecules with metallic nanoparticles, *IEEE J. Sel. Top. Quantum Electron.* **14**, 1430 (2008).
- [60] A. Trügler and U. Hohenester, Strong coupling between a metallic nanoparticle and a single molecule, *Phys. Rev. B* **77**, 115403 (2008).
- [61] K. V. Nerkararyan and S. I. Bozhevolnyi, Relaxation dynamics of a quantum emitter resonantly coupled to a metal nanoparticle, *Opt. Lett.* **39**, 1617 (2014).
- [62] K. V. Nerkararyan, T. S. Yezekyan, and S. I. Bozhevolnyi, Dynamics of a quantum emitter resonantly coupled to both external field and localized surface plasmon, *Phys. Rev. B* **97**, 045401 (2018).
- [63] J. Y. Zhao, Y. Q. Cheng, H. M. Shen, Y. Y. Hui, T. Wen, H. C. Chang, Q. H. Gong, and G. W. Lu, Light emission from plasmonic nanostructures enhanced with fluorescent nanodiamonds, *Sci. Rep.* **8**, 3605 (2018).
- [64] J. Zuloaga, E. Prodan, and P. Nordlander, Quantum description of the plasmon resonances of a nanoparticle dimer, *Nano Lett.* **9**, 887 (2009).
- [65] D. F. Walls, Squeezed states of light, *Nature (London)* **306**, 141 (1983).
- [66] J. Appel, E. Figueroa, D. Korystov, M. Lobino, and A. I. Lvovsky, Quantum Memory for Squeezed Light, *Phys. Rev. Lett.* **100**, 093602 (2008).
- [67] H. P. Yuen and V. W. S. Chan, Noise in homodyne and heterodyne detection, *Opt. Lett.* **8**, 177 (1983).
- [68] R. E. Slusher, L. W. Hollberg, B. Yurke, J. C. Mertz, and J. F. Valley, Observation of Squeezed States Generated by Four Wave Mixing in an Optical Cavity, *Phys. Rev. Lett.* **55**, 2409 (1985).
- [69] G. Breitenbach, S. Schiller, and J. Mlynek, Measurement of the quantum states of squeezed light, *Nature (London)* **387**, 471 (1997).
- [70] D. T. Smithey, M. Beck, M. G. Raymer, and A. Faridani, Measurement of the Wigner Distribution and the Density Matrix of a Light Mode Using Optical Homodyne Tomography: Application to Squeezed States and the Vacuum, *Phys. Rev. Lett.* **70**, 1244 (1993).
- [71] G. Breitenbach, T. Müller, S. F. Pereira, J.-Ph. Poizat, S. Schiller, and J. Mlynek, Squeezed vacuum from a monolithic optical parametric oscillator, *J. Opt. Soc. Am. B* **12**, 2304 (1995).
- [72] A. I. Lvovsky, Squeezed light, in *Photonics*, Volume 1: Fundamentals of Photonics and Physics, edited by D. L. Andrews (John Wiley & Sons, Norwich, UK, 2015), Chap. 5, pp. 121–164.
- [73] C. W. Gardiner, Inhibition of Atomic Phase Decays by Squeezed Light: A Direct Effect of Squeezing, *Phys. Rev. Lett.* **56**, 1917 (1986).
- [74] H. J. Carmichael, A. S. Lane, and D. F. Walls, Resonance Fluorescence from an Atom in a Squeezed Vacuum, *Phys. Rev. Lett.* **58**, 2539 (1987).
- [75] B. R. Mollow, Power spectrum of light scattered by two-level systems, *Phys. Rev.* **188**, 1969 (1969).
- [76] S. Swain, Anomalous Resonance Fluorescence Spectra in a Squeezed Vacuum, *Phys. Rev. Lett.* **73**, 1493 (1994).
- [77] H. J. Carmichael, A. S. Lane, and D. F. Walls, Resonance fluorescence in a squeezed vacuum, *J. Mod. Opt.* **34**, 821 (1987).
- [78] J. Gea-Banacloche, Two-Photon Absorption of Nonclassical Light, *Phys. Rev. Lett.* **62**, 1603 (1989).
- [79] J. Javanainen and P. L. Gould, Linear intensity dependence of a two-photon transition rate, *Phys. Rev. A* **41**, 5088 (1990).

- [80] Z. Ficek and P. D. Drummond, Three-level atom in a broadband squeezed vacuum field. I. General theory, *Phys. Rev. A* **43**, 6247 (1991).
- [81] C. Cabrillo and S. Swain, Interaction Between Two-Level Atoms and a Squeezed Vacuum in a Cavity: Effect on the Mean Photon Number, *Phys. Rev. Lett.* **77**, 478 (1996).
- [82] E. S. Polzik, J. Carri, and H. J. Kimble, Atomic spectroscopy with squeezed light for sensitivity beyond the vacuum-state limit, *Appl. Phys. B* **55**, 279 (1992).
- [83] A. Huck, S. Smolka, P. Lodahl, A. Sørensen, A. Boltasseva, J. Janousek, and U. Andersen, Demonstration of Quadrature-Squeezed Surface Plasmons in a Gold Waveguide, *Phys. Rev. Lett.* **102**, 246802 (2009).
- [84] B. J. Lawrie, P. G. Evans, and R. C. Pooser, Extraordinary Optical Transmission of Multimode Quantum Correlations Via Localized Surface Plasmons, *Phys. Rev. Lett.* **110**, 156802 (2013).
- [85] D. Wang, C. Xia, Q. Wang, Y. Wu, F. Liu, Y. Zhang, and M. Xiao, Feedback-optimized extraordinary optical transmission of continuous-variable entangled states, *Phys. Rev. B* **91**, 121406(R) (2015).
- [86] J. Roßnagel, O. Abah, F. Schmidt-Kaler, K. Singer, and E. Lutz, Nanoscale Heat Engine Beyond the Carnot Limit, *Phys. Rev. Lett.* **112**, 030602 (2014).
- [87] S. Zeytinoğlu, A. İmamoğlu, and S. Huber, Engineering Matter Interactions Using Squeezed Vacuum, *Phys. Rev. X* **7**, 021041 (2017).
- [88] S. Kono, Y. Masuyama, T. Ishikawa, Y. Tabuchi, R. Yamazaki, K. Usami, K. Koshino, and Y. Nakamura, Nonclassical Photon Number Distribution in a Superconducting Cavity Under a Squeezed Drive, *Phys. Rev. Lett.* **119**, 023602 (2017).
- [89] W. Qin, A. Miranowicz, P.-B. Li, X.-Y. Lü, J. Q. You, and F. Nori, Exponentially Enhanced Light-Matter Interaction, Cooperativities, and Steady-State Entanglement Using Parametric Amplification, *Phys. Rev. Lett.* **120**, 093601 (2018).
- [90] S. Zippilli and D. Vitali, Dissipative Engineering of Gaussian Entangled States in Harmonic Lattices With a Single-Site Squeezed Reservoir, *Phys. Rev. Lett.* **126**, 020402 (2021).
- [91] D. Sarid and W. Challener, *Modern Introduction to Surface Plasmons: Theory, Mathematica Modeling, and Applications* (Cambridge University Press, New York, 2010), Chap. 9.
- [92] M. O. Scully and M. S. Zubairy, *Quantum Optics* (Cambridge University Press, Cambridge, 1997).
- [93] S. A. Rastghalam and M. B. Harouni, Interaction between a semiconductor quantum dot microcavity and a squeezed vacuum in a cavity: Effects on the photon statistics, *Laser Phys.* **23**, 115202 (2013).
- [94] S. S. Hassan, A. Joshi, O. M. Frege, and W. Emam, Damping of a harmonic oscillator in a squeezed vacuum without rotating-wave approximation, *Ann. Phys.* **322**, 2007 (2007).
- [95] A. Majumdar, E. D. Kim, Y. Gong, M. Bajcsy, and J. Vučković, Phonon mediated off-resonant quantum dot-cavity coupling under resonant excitation of the quantum dot, *Phys. Rev. B* **84**, 085309 (2011).
- [96] C. W. Gardiner and P. Zoller, *Quantum Noise* (Springer-Verlag, Berlin, 2005).
- [97] C. R. Kagan, E. Lifshitz, E. H. Sargent, and D. V. Talapin, Building devices from colloidal quantum dots, *Science* **353**, aac5523 (2016).
- [98] V. I. Klimov, A. A. Mikhailovsky, S. Xu, A. Malko, J. A. Hollingsworth, C. A. Leatherdale, H. J. Eisler, and M. G. Bawendi, Optical gain and stimulated emission in nanocrystal quantum dots, *Science* **290**, 314 (2000).
- [99] A. Aboulfotouh, M. Fikry, M. Mohamed, M. Omar, H. Rady, and Y. Elbasha, Spectroscopic study of oscillator strength and radiative decay time of colloidal CdSe quantum dots, *Opt. Quantum Electron.* **50**, 115 (2018).
- [100] K. Santhosh, O. Bitton, L. Chuntonov, and G. Haran, Vacuum Rabi splitting in a plasmonic cavity at the single quantum emitter limit, *Nat. Commun.* **7**, 11823 (2016).
- [101] H. Leng, B. Szychowski, M.-C. Daniel, and M. Pelton, Strong coupling and induced transparency at room temperature with single quantum dots and gap plasmons, *Nat. Commun.* **9**, 4012 (2018).
- [102] P. Nagpal, N. C. Lindquist, S. H. Oh, and D. J. Norris, Ultraslow patterned metals for plasmonics and metamaterials, *Science* **325**, 594 (2009).
- [103] L. E. Ocola, Nanoscale geometry assisted proximity effect correction for electron beam direct write nanolithography, *J. Vac. Sci. Technol. B* **27**, 2569 (2009).
- [104] P. W. K. Rothmund, Folding DNA to create nanoscale shapes and patterns, *Nature (London)* **440**, 297 (2006).
- [105] S. M. Douglas, H. Dietz, T. Liedl, B. Hogberg, F. Graf, and W. M. Shih, Self-assembly of DNA into nanoscale three-dimensional shapes, *Nature (London)* **459**, 414 (2009).
- [106] G. P. Acuna, F. M. Möller, P. Holzmeister, S. Beater, B. Lalkens, and P. Tinnefeld, Fluorescence enhancement at docking sites of DNA-directed self-assembled nanoantennas, *Science* **338**, 506 (2012).
- [107] M. P. Busson, B. Rolly, B. Stout, N. Bonod, and S. Bidault, Accelerated single photon emission from dye molecule-driven nanoantennas assembled on DNA, *Nat. Commun.* **3**, 962 (2012).
- [108] E. Cohen-Hoshen, G. W. Bryant, I. Pinkas, J. Sperling, and I. Bar-Joseph, Exciton-plasmon interactions in quantum dot-gold nanoparticle structures, *Nano Lett.* **12**, 4260 (2012).
- [109] T. Hartsfield, W. S. Chang, S. C. Yang, T. Ma, J. W. Shi, L. Y. Sun, G. Shvets, S. Link, and X. Q. Li, Single quantum dot controls a plasmonic cavity's scattering and anisotropy, *Proc. Natl. Acad. Sci. USA* **112**, 12288 (2015).
- [110] D. Ratchford, F. Shafiei, S. Kim, S. K. Gray, and X. Li, Manipulating coupling between a single semiconductor quantum dot and single gold nanoparticle, *Nano Lett.* **11**, 1049 (2011).
- [111] H. Naiki, S. Masuo, S. Machida, and A. Itaya, Single-photon emission behavior of isolated CdSe/ZnS quantum dots interacting with the localized surface plasmon resonance of silver nanoparticles, *J. Phys. Chem. C* **115**, 23299 (2011).
- [112] P. Johnson and R. Christy, Optical constants of the noble metals, *Phys. Rev. B* **6**, 4370 (1972).
- [113] S. Raza, S. I. Bozhevolnyi, M. Wubs, and N. A. Mortensen, Nonlocal optical response in metallic nanostructures, *J. Phys. Condens. Matter* **27**, 183204 (2015).
- [114] C. Leroux, L. C. G. Govia, and A. A. Clerk, Enhancing Cavity Quantum Electrodynamics Via Antisqueezing: Synthetic Ultrastrong Coupling, *Phys. Rev. Lett.* **120**, 093602 (2018).
- [115] J. D. Jackson, *Classical Electrodynamics* (John Wiley and Sons, New York, 1975).
- [116] D. J. Griffiths and R. College, *Introduction to Electrodynamics*, Vol. 3 (Prentice Hall, Upper Saddle River, NJ, 1999).